Experimental Analysis and Modeling of Drag Force: Investigating the Levitation of Spheres in Turbulent Jets

Zhaoyang Yu

Department of Earth Science and Engineering, Imperial College London, South Kensington Campus, SW7 2AZ, London, UK

zhaoyang.yu22@imperial.ac.uk

Abstract. This study investigates sphere levitation and cube instability in turbulent jet flows, examining object geometry, flow rates, and rotational effects. Spheres showed significant variations in hovering height with changing flow rates, ranging from 355.5 mm at 41.1 L/s to 92.5 mm at 28.0 L/s. Measurement errors spanned from 1.2% to 17.1%, highlighting challenges in predicting complex fluid-structure interactions. Rotational motion enhanced hovering heights through Magnus forces but increased instability. Cubes exhibited inherent instability due to sharp edges causing early boundary layer separation, resulting in a brief hovering period of 0.167 seconds. X-axis rotation at 0.2 seconds further reduced lift and accelerated descent. The findings emphasize the critical role of object geometry and rotational dynamics in levitation behavior within turbulent jet flows. Future research will focus on refining drag coefficient calculations, analyzing surface pressure distributions, and validating findings through CFD simulations. These efforts aim to enhance understanding of flow-structure interactions in high-turbulence environments, with potential applications in aerodynamics, industrial processes, and environmental studies.

Keywords: Levitation of Spheres，turbulent jet flows,object geometry, flow rates, rotational effects, CFD simulation.

1. Introduction

Levitation is a fascinating phenomenon that demonstrates the balance of forces acting on an object in motion.This report focuses on the levitation of spherical objects in an upward turbulent jet and aims to measure the equilibrium height under different conditions. Turbulent jet levitation occurs when a high-speed jet interacts with an object, creating a stable hovering state due to the balance of drag force, gravity, and turbulence-induced pressure[1]. This process depends on factors such as the object's weight, shape, and the properties of the airflow, including its velocity and turbulence level[2]. Spheres are the primary focus of this study because their symmetry simplifies the analysis of aerodynamic forces.A key factor in stabilizing the sphere is the Coanda effect,which generates a restoring force that keeps the sphere centered in the jet[3]. To broaden the scope, the study also investigates non-spherical objects like cubes to explore how sharp edges and irregular shapes affect stability.

This work has two main objectives: first, to determine how the weight and diameter of spheres affect their levitation height; second, to compare the experimental results with theoretical models of drag and turbulence. A high Reynolds number jet is used, as its well-defined velocity profile and conical fow shape are ideal for such experiments[4]. The fow rate plays a crucial role, needing to exceed a certain threshold to support levitation.At higher fow rates, turbulence can destabilize the sphere or even eject it from the jet. Non-spherical objects introduce additional challenges, as sharp edges can disrupt the airflow, causing instability and rapid descent.

The results of this study aim to bridge the gap between theoretical predictions and experimental observations, providing practical insights into how shape, weight, and fow properties interact during levitation. This work also suggests improvements for existing models by incorporating rotational effects, turbulence, and boundary layer behavior, contributing to a deeper understanding of levitation dynamics.

2. Methods

Three experiments with different airflow speeds and one control group using a cube of equivalent mass were conducted to investigate this topic.

2.1. Background Theory

2.1.1 Turbulent Jet Flow

A turbulent jet flow is characterized by the mixing of high-momentum fluid with the surrounding low-momentum fluid, resulting in velocity fluctuations and turbulence across the jet. The velocity distribution within a turbulent jet follows a self-similar profile, where the velocity at any radial position r and downstream distance x can be expressed as[2]:

$$u(x,r) = U_{\max} exp\left(-\frac{r^2}{2\sigma^2}\right), \tag{1}$$

where $U_{\max}$ is the maximum velocity at the centerline, and $\sigma(x)$ represents the standard devi- ation of the velocity distribution, which increases linearly with x as:

$$\sigma(x) = \frac{x}{10}.$$

The centerline velocity decreases with distance according to:

$$U_{\max} = \frac{5U_0 d}{x}$$

where U_0 is the jet velocity at the nozzle exit and d is the nozzle diameter. The radius of the jet grows linearly as:

$$R(x) = \frac{x}{5}.$$

2.1.2 Turbulent Boundary Layer

A turbulent boundary layer forms when fluid flows over a solid surface at high Reynolds numbers, where inertial forces dominate over viscous forces [5]. The growth of the boundary layer thickness can be expressed as:

$$\frac{\delta}{x} = 0.37 Re_x^{-1/5}, \tag{2}$$

where Re_x is the Reynolds number based on the streamwise position x:

$$Re_{x_{cr}} = \frac{\rho U x_{cr}}{\mu}. \tag{3}$$

Turbulent boundary layers exhibit higher velocity gradients near the wall and higher wall shear stresses compared to laminar layers. Hence, they are more resistant to flow separation and significantly influence the forces acting on objects within the boundary layer.

2.2. Data Collection

The airflow source is a Dyson HD07 Supersonic hair dryer, placed horizontally on a 0-degree inclined plane with the heating temperature set to 0. The volume flow rates for the three airflow speed settings were measured using a 30L trash bag and determined to be 41.1 L/s, 33.0 L/s, and 28.0 L/s, respectively (Table 1). After turning on the hair dryer, a sphere with a diameter of 40 mm, a mass of 2.7 g, and made of ABS (molded) was placed in the airflow at each of the three speed settings. Once stabilized, the sphere was released to move freely. Subsequently, a cube with a side length of 25 mm and the same mass was tested under the airflow with a flow rate of 41.1 L/s as a control experiment

to compare with the sphere under identical conditions. The entire process was recorded using a smartphone in 2K resolution at 60 frames per second, with an actual frame rate of 59.94 fps.

2.2.1 Error Analysis

If Q is a function $f(x_1, x_2, \ldots, x_n)$,the total uncertainty ΔQ can be expressed as[6]:

$$\Delta Q = \sqrt{\sum_{i=1}^{n} \left(\frac{\partial f}{\partial x_i} \Delta x_i\right)^2}$$

$\frac{\partial f}{\partial x_i}$: The partial derivative of f with respect to input variable x_i Δx_i: The uncertainty in the input variable x_i. The fow rate Q was calculated using the formula:

$$Q_{(\mathrm{V,t})} = \frac{V}{t}$$

where V is the volume of the trash bag (30 L) and t is the time recorded for the bag to fill.

The error in the flow rate can be estimated using the equation:

$$\Delta Q_{(\mathrm{V,t})} = Q\sqrt{\left(\frac{\Delta V}{V}\right)^2 + \left(\frac{\Delta t}{t}\right)^2}$$

ΔV: Uncertainty in the volume. Assumed to be ± 0.5L based on the bag's measurement precision and airtightness. Δt： Uncertainty in the stopwatch timing. assumed to be ± 0.01 S.

3. Processing

Using the Tracker software [6] on a Win64 system, the video encoded in MP4 (H264 + AAC) format was imported into the software. A stationary background object was selected to set a calibration stick and confirm the length scale, followed by setting the origin of the coordinate system at the center of the hair dryer outlet. The frames required for the experiment were selected, starting from the release frame and ending with the frame where the target completed one full cycle of motion. The track function was enabled, and point mass was selected with the target's mass set. Starting from the initial frame, the centroid of the target object was located frame by frame (Fig 1).

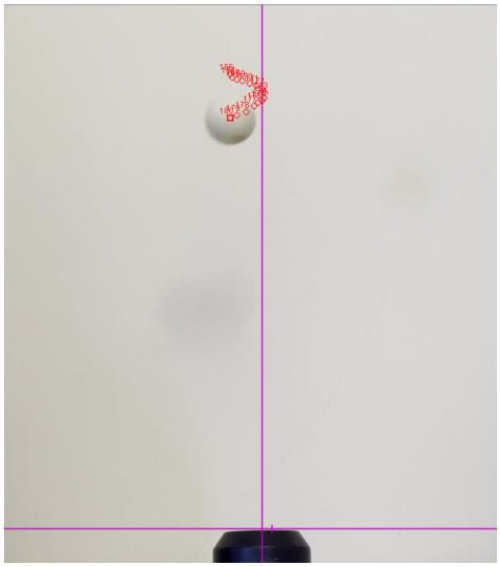

Figure 1: Result after implementing track mode

Subsequently, the data in the attribute table was selected and imported into the analysis module. The data was further analyzed, and error was calculated (Fig 2) using Python.

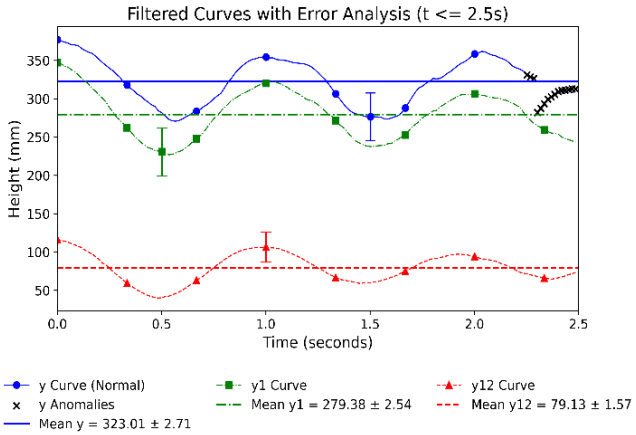

Figure 2: The curves were plotted starting from the first peak point, and subsequently shifted to begin at $x = 0$ for a more intuitive comparison. The y_{12} curve corresponds to a flow rate of 28 L/s, the y_1 curve corresponds to a flow rate of 33 L/s, and the y curve corresponds to a flow rate of 41.1 L/s. Further error analysis was conducted accordingly.

3.1. Error Analysis

The following formulas were used for data analysis and error estimation [7].

The meaning represents the average value of a dataset and is calculated as

$$\text{Mean} = \frac{\sum_{i=1}^{n} x_i}{n}$$

where x_i represents each data point, and n is the total number of data points

The standard deviation quantifies the amount of variation or dispersion in the dataset. It is defined as:

$$\sigma = \sqrt{\frac{\sum_{i=1}^{n}(x_i - \text{Mean})^2}{n}}$$

A higher standard deviation indicates greater variability among the data points.

The uncertainty in the mean estimates the precision of the calculated mean and depends on the standard deviation and the number of data points. It is given by:

$$\text{Uncertainty in Mean} = \frac{\sigma}{\sqrt{n}}$$

This formula reflects how the uncertainty decreases with a larger number of measurements (n).

4. Results and Discussion.

From the initial observation of the plots, it was hypothesized that the motion could be approximated using a damped harmonic oscillation model. The following model was used to fit the data:

$$y(t) = A \cdot e^{-\gamma t} \cdot \cos(\omega t + \phi) + C \tag{4}$$

A: Initial amplitude: Damping coefficient, representing the rate of decay. ω: Angular frequency. ϕ: Phase. C: Equilibrium position.

The above parameters were extracted from the fitted model shown in Table 2. The fitted results were overlaid with the original data to visually compare and evaluate the accuracy of the model.

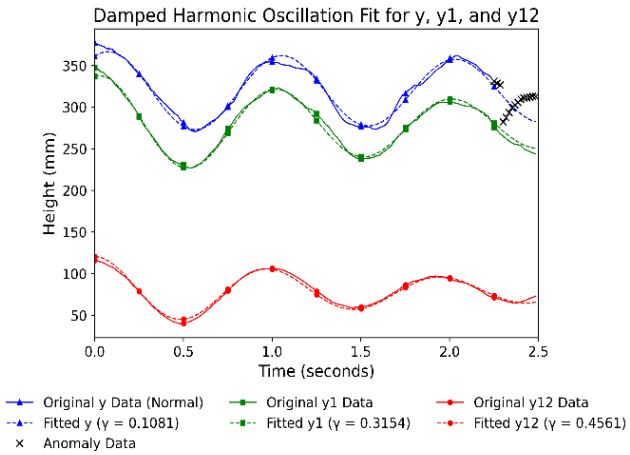

Figure 3: Interpolate for damp harmonic oscillation, y data anomalies are marked.

Steady State Analysis

The radial velocity distribution is described in equation (1) and rewritten to satisfy the current coordinate axes. The boundary layer thickness accounts for reducing effective jet velocity near the ball surface. The Reynolds number and boundary layer thickness are described in equation (2)(3) and rewritten. The speed is averaged over the front-facing hemisphere to compute the effective jet velocity over the sphere's surface:

$$u_{\text{surface}}(y)=\frac{1}{A_{\text{proi}}}\int_{-\pi/2}^{\pi/2} U_{\max}(y)\cdot\exp\left(-\frac{(r\cos\theta)^2}{2\sigma^2(y)}\right)\cos\theta d\theta \tag{5}$$

The effective jet velocity further accounts for the boundary layer effect:

$$u_{\text{eff}}(y)=u_{\text{surface}}(y)\cdot\left(1-\frac{\delta(y)}{y}\right) \tag{6}$$

The relative velocity between the sphere and the air is:

$$v_{\text{rel}}=u_{\text{eff}}(y)-v$$

The drag force experienced by the sphere is then:

$$F_a=\frac{1}{2}\rho C_d A_{\text{proj}} v_{\text{rel}}^2$$

The sphere's vertical motion is governed by Newton's second law:

$$m\frac{d^2y}{dt^2}=F_a-F_g \tag{7}$$

Substituting the expressions for drag and gravity:

$$\frac{d^2y}{dt^2}=\frac{1}{2m}\rho C_d A_{\text{proj}}\left(u_{\text{eff}}(y)-v\right)^2-g, \quad \text{where } v=\frac{dy(t)}{dt} \text{ as described in equation(4).} \tag{8}$$

The initial contact of the gas with the front surface of the sphere causes a reduction in velocity, creating a high-pressure region. On the leeward side, boundary layer separation results in turbulence, while the accelerated airflow along the lateral surfaces generates a low-pressure region, further balancing the sphere's own weight. For the sphere's stability in the airflow, the low-pressure region caused by the increased flow velocity on one side, due to positional displacement, pulls the sphere back toward the center of the airflow. When switching to higher wind power (from 33 L/s to 41 L/s), the reduction in vertical displacement might be attributed to more fully developed turbulence at

greater y distances and the attenuation of airflow velocity, thereby failing to provide a linearly increasing lifting force. The preliminary model has been shown to effectively response to the positional variation in the y-axis direction as the time shifts(without considering rotational effects). The theoretical and experimental parameters of the damped SHM model reveal notable discrepancies, particularly in the amplitude (A), damping coefficient (γ), angular frequency (ω), and steady-state height (C). The experimental results for U_0 = 27.03 m/s, U_0 = 21.71 m/s, and U_0 = 18.41 m/s are 48.51 mm, 60.36 mm, and 41.97 mm, respectively. The theoretical amplitude is underrepresented, approximately 30-40 mm. This underestimation likely stems from the theoretical model's inability to fully account for the experimental release conditions and initial disturbances. The experimental values vary significantly with flow velocity, with γ_{exp} = 0.1081, 0.3154, and 0.4561 for U_0 = 27.03 m/s, U_0 = 21.71 m/s, and U_0 = 18.41 m/s, respectively. In contrast, the theoretical model implicitly represents damping through the drag force (F_a), but the resulting effective damping is smaller in the range of 0.07-0.1. This discrepancy may cause by the model's lack of consideration of rotational effects and energy dissipation from turbulence. The angular frequency derived from the experimental data shows consistency across all flow velocities, with values close to 6.4 rad/s. The theoretical angular frequency matches this, as it is determined by the balance of aerodynamic forces and gravity.

The experimental values for the steady-state height for the three flow velocities are 323.01 mm, 279.38 mm, and 79.13 mm, respectively, while the theoretical values are 355.5 mm, 275.7 mm, and 92.5 mm. The relative errors are 10.1%, 1.2%, and 17.1%, respectively. The steady-state height is well-predicted at moderate flow velocities but overestimated at low flow rates due to the model's simplified treatment of turbulence and boundary layer separation, which reduces the effective lift in experimental settings.

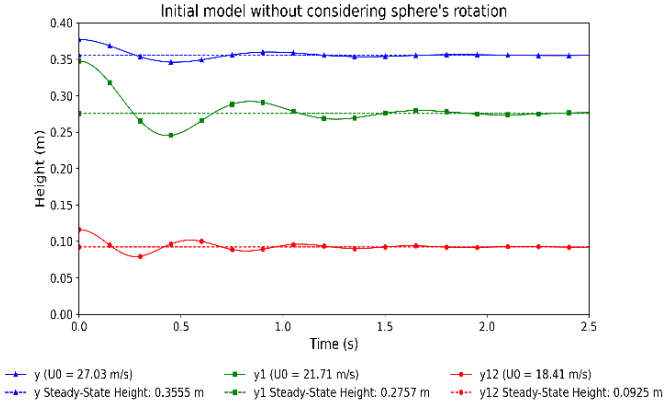

Figure 4: Parameters used to simulate: velocity is calculated using volume flow rate, air density $\rho = 1.225\text{kg/m}^3$, drag coefficient $C_d = 0.4$ (assumed), projected area of the sphere $A_{\text{proj}} = \pi \times (0.02)^2\text{m}^2$ (sphere radius r =0.02 m),mass of the sphere $m = 0.0027$ kg gravitational acceleration $g = 9.81\text{m/ } s^2$, jet nozzle diameter $d = 0.044\text{m}$, virtual origin offset $y_0 = 0.05\text{m}$ and dynamic viscosity of air $\mu = 1.8 \times 10^{-5}\text{Pa·s}$

Figure 4: Parameters used to simulate: velocity is calculated using volume flow rate, air density ρ = 1.225kg/m^3, drag coefficient C_d = 0.4 (assumed), projected area of the sphere $A_{\text{proj}} = \pi (0.02)^2$ m^2 (sphere radius r = 0.02 m), mass of the sphere m = 0.0027 kg, gravitational acceleration g = 9.81 m/s^2, jet nozzle diameter d = 0.044 m, virtual origin offset y_0 = 0.05 m, and dynamic viscosity of air $\mu = 1.8 \times 10^{-5}$ Pa·s.

Considering Rotation

The lift coefficient $C_{L\Omega}$ for a spinning sphere in viscous flow, as a function of the Reynolds number (Re) and the dimensionless spin ratio (Rr), is given by [8]:

$$C_{L\Omega} = 0.365(1+e^{2.229-6.5Rr})^{-1} + \left[Rr - 0.365(1+e^{2.229-6.5Rr})^{-1}\right] e^{-0.075(0.5Rr)^{0.4}Re^{0.71}}$$

The Magnus force due to sphere rotation is:

$$F_m = \frac{1}{2}\rho C_l A \omega v_{\text{rel}}$$

The sphere's vertical motion is governed by Newton's second law and refined by Magnus force:

$$m - \frac{d^2y}{dt^2} = F_d + F_m - F_g \tag{9}$$

Substitute the expressions for drag, Magnus force, and gravity:

$$\frac{d^2y}{dt^2} = \frac{1}{2m}\rho C_D A\left(u_{\text{eff}}(y) - v\right)^2 + \frac{1}{2m}\rho C_l A\omega\left(u_{\text{eff}}(y) - v\right) - g, \quad \text{where } v = \frac{dy(t)}{dt} \tag{10}$$

The sphere's angular velocity ω evolves due to the torque exerted by the airflow:

$$I\frac{d\omega}{dt} = \tau$$

The torque τ is related to the drag force as:

$$\tau = krF_a$$

where k is an empirical coefficient accounting for the torque's dependency on the sphere's geometry and flow distribution, where $I = \frac{2}{5}mr^2$ is the moment of inertia for a solid sphere. Thus, the coupled system of equations governing the sphere's motion and rotation is:

$$\frac{d^2y}{dt^2} = \frac{1}{2m}\rho C_D A\left(u_{\text{eff}}(y) - v\right)^2 + \frac{1}{2m}\rho C_l A\omega\left(u_{\text{eff}}(y) - v\right) - g \tag{11}$$

$$\frac{d\omega}{dt} = \frac{kr}{I}\cdot\frac{1}{2}\rho C_D A\left(u_{\text{eff}}(y) - v\right)^2 \tag{12}$$

Introducing preliminary rotation shows that the steady-state hovering height of the sphere increases significantly with increasing flow velocity, likely due to the enhancement of the low-pressure region. Additionally, a simple damped oscillation no longer converges to a fixed height.

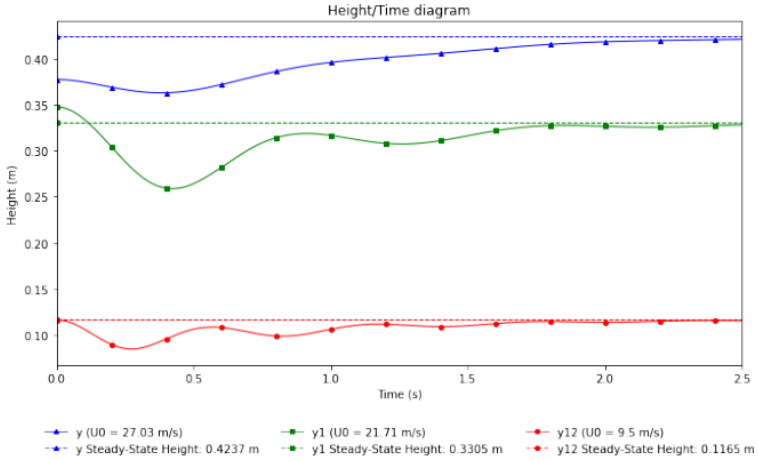

Figure 5: Fitting result considering sphere's rotation and uses same parameters as previously discussed.

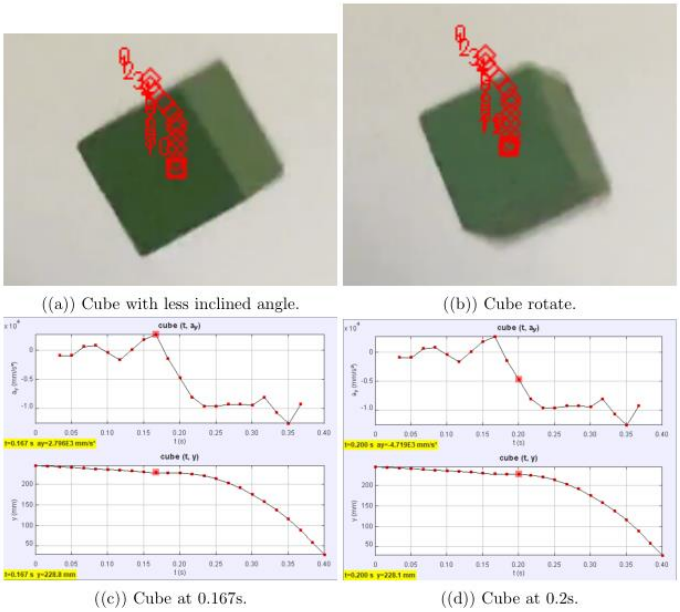

Figure 6: Four-panel layout of cube-related images: (a) Cube image, (b) Cube rotate, (c) Cube at 0.2s, and (d) Cube example.

From the angular velocity plot, it can be observed that the rotational speed continues to increase and approaches a constant value. This occurs because the increase in height reduces the influence of airflow intensity on the sphere's rotation, thereby decreasing the acceleration of angular velocity. This phenomenon arises because the report does not account for oscillations in the x-direction. Without considering variations along the x-axis, lateral movement alters the airflow velocity along the sphere's curved surface, changing the sphere's rotational speed during motion. As a result, the angular velocity decreases rather than continuously accelerating as predicted by theoretical models. Admittedly, the considerations of turbulence and boundary layer effects remain overly simplistic in this analysis. Further studies will require Computational Fluid Dynamics data for a more comprehensive understanding.

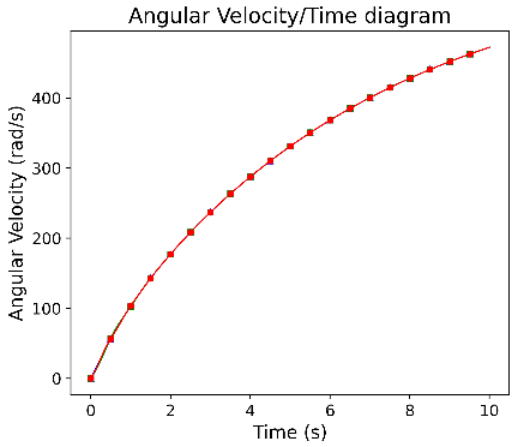

Figure 7: Angular velocity derived from 3 data lines.

Additionally, the experiment included a cube of the same mass under a 41 L/s airflow. The sharp edges of the cube caused premature and more significant boundary layer separation, preventing the formation of a stable flow field and rendering simple symmetric models inapplicable. The model's lift calculation assumes smooth airflow around the curved surface of a sphere, and rotation cannot be explained by the Magnus effect. The turbulence around the cube is more intense and less predictable. The model predicts that the cube's rotational stability is insufficient to generate sustained lift, and any displacement from the airflow center would fail to produce corrective forces, leading to a fall.

This was confirmed experimentally: after release, a smaller tilt angle at 0.167 s (Fig.7(a)) slowed the descent, generating positive acceleration along the y-axis (Fig.7(c)). From the y-axis versus the time curve, it is evident that between 0.15 s and 0.2 s, a reduced descent velocity caused a brief near-hovering state. At 0.2 s, a noticeable x-axis rotation (Fig.7(b)) increased the number of edges facing the airflow, significantly decreasing the high-pressure region and lift, resulting in a rapid descent (Fig.7(d)). From 0.234 s to 0.3 s, the cube ceased further rotation and continued descending at its current acceleration.

To optimize the model, the drag coefficient for the cube must be recalculated, and lift should be derived by integrating the normal pressure over its surfaces. For rotation, angular velocity corrections should be incorporated, followed by model refinement using results from numerical simulations [9-10].

5. Conclusion

The experimental study highlights the dynamics of sphere levitation and cube instability in turbulent jets. For spheres, the steady-state height modelling showed clear dependency on flow rates: 355.5 mm at 41.1 L/s, 275.7 mm at 33.0 L/s, and 92.5 mm at 28.0 L/s, with theoretical errors ranging between 1.2% and 17.1%. Rotational effects increased the hovering height significantly, though damping oscillations no longer converged, suggesting the enhancement of low-pressure regions from Magnus force. The cube, under 41 L/s, exhibited instability caused by premature boundary layer separation due to sharp edges. At 0.167 s, the reduced tilt angle slowed its descent momentarily, but the x-axis rotation at 0.2 s increased edge exposure, reducing lift and accelerating its fall. Between 0.234 s and 0.3 s, the cube stabilized in its rotation but continued descending. To refine models for cubes, recalculation of drag coefficients and surface pressure integration are recommended, with CFD data to validate turbulent and boundary effects.

References

[1] T. Barois, G. Ricard, V. Champain, L. Gey, and H. Kellay, "The levitation of a sphere by two parallel turbulent jets," *Physics of Fluids*, vol. 32, no. 4, p. 045111, 2020.

[2] [G. N. Abramovich, T. A. Girshovich, S. Iu. Krasheninnikov, A. N. Sekundov, and I. P. Smirnova, *The Theory of Turbulent Jets (2nd Revised and Enlarged Edition)*, Moscow: Izdatel Nauka, Jan. 1984.

[3] D. J. Tritton, *Physical Fluid Dynamics*, reprinted 1980 ed., Van Nostrand Reinhold, 1977.

[4] H. J. Hussein, S. P. Capp, and W. K. George, "Velocity measurements in a high-Reynolds-number, momentum-conserving, axisymmetric, turbulent jet," *Journal of Fluid Mechanics*, vol. 258, pp. 31–75, 1994.

[5] H. Schlichting and K. Gersten, *Boundary Layer Theory*, 9th ed., Berlin, Heidelberg: Springer, 2017.

[6] D. Brown, "Tracker: Video analysis and modeling tool," Open-Source Physics Project, 2023.

[7] J. R. Taylor, *An Introduction to Error Analysis: The Study of Uncertainties in Physical Measurements*, 2nd ed., Sausalito, CA: University Science Books, 1997.

[8] S. Zhou, G. Zhang, and X. Xu, "Experiments on the drag and lift coefficients of a spinning sphere," *Water*, vol. 14, no. 17, 2022.

[9] B. Mele, M. Ostieri, and R. Tognaccini, "Aircraft lift and drag decomposition in transonic flows," *Journal of Aircraft*, vol. 54, no. 1, pp. 120-131, Jan. 2017.

[10] C. Marongiu, R. Tognaccini, and M. Ueno, "Lift and lift-induced drag computation by Lamb vector integration," *AIAA Journal*, vol. 51, no. 6, pp. 1309-1321, Jun. 2013.